Icarus 389 (2023) 115272

Contents lists available at ScienceDirect

Icarus

journal homepage: www.elsevier.com/locate/icarus

Exploring the variability of the venusian thermosphere with the IPSL Venus GCM

Antoine Martinez [a,*], Sébastien Lebonnois [a], Ehouarn Millour [a], Thomas Pierron [a], Enora Moisan [a], Gabriella Gilli [b,c], Franck Lefèvre [d]

[a] Laboratoire de Météorologie Dynamique, UMR 8539, IPSL, CNRS, Sorbonne Université, Paris, France
[b] Instituto de Astrofísica de Andalucia (IAA-CSIC), Glorieta de la Astronomia s/n, Granada, Spain
[c] Instituto de Astrofisica e Ciencias do Espaço (IA), OAL, Tapada da Ajuda, PT1349-018 Lisboa, Portugal
[d] LATMOS, CNRS, Sorbonne Université, Université Versailles St-Quentin, Paris, France

ARTICLE INFO

Keywords:
Venus
Thermosphere
Modeling
Composition
Solar cycle

ABSTRACT

Recent simulations of the Institut Pierre-Simon Laplace (IPSL) Venus Global Climate Model (VGCM) developed at the Laboratoire de Météorologie Dynamique (LMD) were performed with a model top raised from ~10^{-5} (~150 km) to ~10^{-8} Pa (180–250 km; upper boundary). The parameterizations of non-LTE CO_2 near infrared heating rates and of non-orographic gravity waves were improved. In addition, a tuning of atomic oxygen production was introduced to improve related effects (heating and cooling) and resulting thermospheric number densities. This work focusses on validating the modelled thermospheric structure using data from the Pioneer Venus, Magellan and Venus Express missions which cover similar and complementary (equator and pole) regions at different periods of solar activity, typically above altitudes of 130 km. This version of the IPSL VGCM shows good agreement with the diurnal evolution of the exospheric temperature at the equator reconstructed from the atomic oxygen scale height of the Pioneer Venus Orbiter Neutral Mass Spectrometer data. The model is also able to reproduce the sensitivity of the exospheric temperature and species density to the EUV flux of the solar high activity period (from 180 to 230 solar flux unit; s.f.u). However, to fit with the PV-ONMS density observations, it was necessary to increase the photodissociation of CO_2 into CO and O above 135 km by a factor of 10. Indeed, our study points to the importance of an additional source of oxygen and carbon monoxide production above 130 km other than CO_2 photolysis to explain the vertical profiles of CO and O number density in the thermosphere. Moreover, the presence of a GW drag at altitudes above 140 km has a significant impact on the nightside temperature value and its distribution.

1. Introduction

In the last decade, General Circulation Models (or Global Climate Models, GCM) have made important progress in predicting and understanding the characteristics of the Venusian atmosphere, from the deep atmospheric structure to the thermospheric activity (e.g. Brecht et al., 2011; Hoshino et al., 2013; Sugimoto et al., 2014; Lebonnois et al., 2016; Mendonça and Read, 2016; Yamamoto, 2019). Among these models, the IPSL VGCM presents many advantages. It is the first model to include the change of specific heat with temperature, $C_p(T)$, a significant property that affects the definition of the potential temperature and therefore the stability structure of the atmosphere (Lebonnois et al., 2010, 2016). The lower atmosphere (surface to cloud-top) was investigated and compared to observations, in particular the thermal structure in the cloud layer (Garate-Lopez and Lebonnois, 2018; Scarica et al., 2019). The impact of topography on the circulation near the cloud-top was studied and the stationary features known as the bow-shaped waves observed by Akatsuki (Kouyama et al., 2017) were reproduced with an orographic gravity wave parameterization (Navarro et al., 2018). The IPSL VGCM also includes a fully-coupled photochemical model and a simplified cloud model implemented up to 150 km (Stolzenbach et al., 2014, 2015; Gilli et al., 2017). This vertical extension is a crucial advantage to model the connection between regions below the clouds and above the clouds through planetary-scale wave activity and small-scale gravity waves generated by the middle-cloud convective region. The upper atmosphere is therefore fully connected to the cloud region and deep atmosphere

* Corresponding author.
E-mail address: antoine.martinez@lmd.ipsl.fr (A. Martinez).

https://doi.org/10.1016/j.icarus.2022.115272
Received 19 January 2022; Received in revised form 12 September 2022; Accepted 14 September 2022
Available online 21 September 2022

dynamical activity. Among the recent developments, the thermal structure in the 90–150 km altitude region has recently been improved through tuning of the non-LTE CO_2 heating rate parameterization, and of the convectively-generated gravity wave parameterization (Gilli et al., 2017, 2021; Navarro et al., 2021). All the physics needed to reach the exobase have been implemented, so the upper boundary was recently extended up to 10^{-8} Pa (approximately 250 km altitude at noon and 180–200 km altitude on the nightside).

Based on the simulations provided by the IPSL VGCM, our team is now ready to offer access to a reference climatological model for use by the scientific community that study the atmosphere of Venus and by engineers that develop mission designs and instrumentation for Venus exploration. Such a tool has been made available for nearly twenty years in the case of Mars exploration: the Mars Climate Database (MCD) is used worldwide. The Venus Climate Database (VCD) is now available (see http://www-venus.lmd.jussieu.fr), and provides a climatology (mean values and variability) for many characteristics of the Venusian atmosphere from the surface to the exosphere, validated against available observations.

In order to provide a modelled atmosphere reproducing as closely as possible to the observations, a few adjustments were done to the GCM basic processes in the context of the VCD. These tunings are detailed in the present work and these simulations provide the fields included in the VCD 2.0. To validate the model and tuning, measurements from several missions were used: Firstly, the Pioneer Venus Orbiter data with the number density of He, CO, O, CO_2, N and N_2 at the equator during the high solar activity from 1978 to 1980 (Niemann et al., 1980). Secondly, mass density observations from Pioneer Venus Orbiter (Keating et al., 1985; Tolson et al., 2013), Magellan (Giorgini et al., 1995; Tolson et al., 2013) and Venus Express (Persson, 2015; Müller-Wodarg et al., 2016; Rosenblatt et al., 2012) aerobraking campaigns around the equator and at the poles for respectively maximum and minimum-intermediate solar cycle conditions.

Section 2 presents the latest additions and improvements made in this version of the model. Comparison to temperature, mass and number density observational data by Pioneer Venus, Magellan and Venus Express missions are done in Section 3. Section 4 discusses the effects of the non-orographic gravity waves parameterization. Conclusions are given in Section 5.

2. Model description and recent improvements

The IPSL VGCM has been used to investigate all regions of the Venusian atmosphere as it covers the surface up to the lower thermosphere (140–160 km; Lebonnois et al., 2010, 2016). The vertical grid was recently extended from 78 to 90 levels (180–250 km) using the vertical extension method detailed in Gilli et al. (2017). The horizontal resolution is 3.75° x 1.875° (96 longitudes × 96 latitudes) and the vertical grid has 90 pressure levels covering from ~$9.2{\cdot}10^{6}$ Pa to ~$8{\cdot}10^{-9}$ Pa. The vertical model resolution is approximately ~2–3 km between 100 and 150 km, slightly smaller below 100 km and ~4–10 km above 150 km (0.01–0.4 scale height below 100 km and 0.4–0.8 scale height above). Conditions at the model upper boundary are similar to previous versions of the IPSL VGCM (sponge layer over the top four layers, with horizontal winds forced towards zonal average fields with timescale of the order of 1 Earth day in the top layer).

Parameterizations for CO_2-O 15-μm cooling, non-LTE CO_2 near infrared heating, thermal conduction, molecular viscosity, extreme ultraviolet (EUV) heating and non-orographic gravity wave (GW) processes are presented and discussed in more detail in Gilli et al. (2017, 2021). In this section the update of the GW, the update of the non-LTE CO_2 near infrared heating parameterizations and the tuning of the upper thermosphere are presented.

2.1. Recent improvements

Since the previous IPSL VGCM version described in Gilli et al. (2021), several updates have been included in the EUV flux proxy, the non-LTE parameterization of the near infrared heating rate, the gravity wave (GW) parameterization and on the vertical grid.

The orbit of Venus has a very low eccentricity (e = 0.0067) and a low obliquity (−2.63°). For these reasons, the seasonal effects on the atmosphere of Venus are weaker than for Mars or the Earth, and neglected in the IPSL VGCM simulations by setting the solar declination angle to zero. One of the main external sources of variability in the Venus thermosphere is the variation in solar ultraviolet and extreme ultraviolet radiation following the 11-year solar cycle and the rotation of the sun (28.6 Earth days for Venus). As for Earth, the solar fluxes responsible for the heating of Venus' upper atmosphere are mostly in the extreme ultraviolet (EUV) range of the solar spectrum. It is common to use the 10.7 cm radio flux (designated F10.7) as a proxy for EUV, as both emissions are thought to originate in the Sun's corona, and therefore to be highly correlated in time (Tobiska et al., 2000). E10.7 is another proxy for EUV flux and is the integrated solar EUV energy flux between 1.8 and 105 nm at the top of the atmosphere, reported in units of 10.7 cm radio flux. Tobiska (2003) showed, by studying the altitude decay for the Solar Mesosphere Explorer satellite that the F10.7 index tends to overestimate the fluctuations of the solar EUV flux, thus producing an over or underestimation of the deposition of EUV energy (including heating) in the thermosphere between 100 and 1000 km, while the E10.7 index manages to reproduce the deposition of EUV energy better. For this reason, the E10.7 index is now used to characterize the solar EUV input in our comparison to the observations, as its temporal fluctuations are closer to the real fluctuations of the energy deposition. Here, for the E10.7 solar flux values, the Solar Irradiance Platform v2.37 solar flux model is adopted (SIP; formerly SOLAR2000; https://spacewx.com/sip/). The E10.7 solar flux is adjusted for the Earth-Sun-Venus angle but remains standardised to 1 AU. For information, the minimum solar cycle period has E10.7 values of 70–100 s.f.u, while the maximum solar cycle period can have values ranging to over 180–220 s.f.u. 140 s.f.u is a reference value for the medium solar cycle period.

The absorption of solar radiation in the non-LTE CO_2 near infrared bands has a considerable impact on the thermal structure of the Venusian atmosphere between 90and 150 km altitude. Roldán et al. (2000) is the reference study on the absorption of solar radiation on Venus, that presents the non-LTE radiative transfer line-by-line model, and shows that this process depends mainly on the density of the atmosphere. The solar zenith angle, the thermal structure and the atomic oxygen abundance have also an influence but with a smaller degree. In the previous version of the IPSL VGCM, for the solar heating calculations, a 1-parameter formula was used, mimicking the essentials of the detailed heating rate calculated by line-by-line non-LTE simulations in Roldán et al. (2000), as done for the Martian atmosphere in Forget et al. (1999) and González-Galindo et al. (2009). Gilli et al. (2021) adapted this near infrared heating rate parameterization to better fit Venus Express temperature observations between 90and 150 km altitude in particular SOIR and SPICAV temperature measurements at the terminator and nighttime respectively. However, this showed an overestimation of the temperature by 20–40 K between 85 and 105 km altitude and an underestimation of the temperature by 20–30 K between 125 and 135 km. In order to improve the temperature profile, the infrared heating rate parameterization used in the IPSL VGCM was reformulated from a single-band heating rate to a multi-band heating rate based on the near infrared heating rate profile presented in Roldán et al. (2000). To do this, the previous heating rate formulation was adapted to add a parameterization for each heating band. This new parameterization is detailed in Appendix A. However, the heating rate profile from Roldán et al. (2000) is subject to uncertainties because the temperature and number density input in this model are based on the VIRA model (Keating et al., 1985; Seiff et al., 1985) and on VTS3 (Hedin et al., 1983)

oxygen abundance. The more recent observations from Venus Express showed that VIRA and VTS3 are not representative of the atmospheric temperature profile of Venus between 90 and 150 km altitude (Limaye et al., 2017). Use of the new temperature measurements in a new study of the near infrared radiative transfer based on a line-by-line model is clearly needed to improve our knowledge of the non-LTE CO_2 near infrared heating rates.

As in previous IPSL VGCM studies of the upper atmosphere, impact of the non-orographic small-scale gravity waves on the Venusian atmospheric circulation is based on the formalism developed for the Earth GCM and fully described in Lott et al. (2012) and Lott and Guez (2013). Theoretically, these gravity waves are expected to be produced near the top of the convective layer of the middle cloud region (approximately 50–60 km altitude). They propagate upward and provide momentum and energy by dissipating in the thermosphere. The effect of gravity waves (GW) on the distribution and variations of wind velocity in the Venusian thermosphere was studied by several GCMs (Bougher et al., 1988; Zalucha et al., 2013; Hoshino et al., 2013; Gilli et al., 2021). In Gilli et al. (2021), the authors show a clear asymmetry of the Subsolar-Antisolar (SS-AS) zonal flow between the morning and the evening branches and at altitudes above 100 km, caused by the Kelvin wave impact but also by non-orographic GW.

The changes made to the near infrared heating rates (described in Appendix A) modified the wind distribution and velocity, which disturbed the propagation of non-orographic gravity waves in the thermosphere, reducing their drag effect on the thermospheric winds. The main impact of this change was a significant increase of the temperature on the night side compared to Gilli et al. (2021) due to dynamical processes as the transfers from the day side to the night side were not slowed down enough anymore. Moreover, these gravity waves were no longer propagating on the evening side above 0.1–0.001 Pa around the equator and above 10^{-4} Pa in polar regions. Yet, in Persson (2015), several Venus Express torque observations show the presence of gravity wave propagation at altitudes above 160–200 km, at latitudes above 75° and at terminator. So, the aims of this update of the GW parameterization were to increase the GW drag and to increase their altitude of propagation above 10^{-4} Pa (approximately 145 km altitude) in order to slow the wind velocity in the thermosphere. The GW parameterization, described in Gilli et al. (2021), is based on key tuneable parameters and was modified as presented in Table 1.

Controlling the decay of the Eliassen Palm (EP) flux, the diffusion parameter is related to the kinematic viscosity $\upsilon = \mu/\rho$, where ρ is the mass density and μ is the dynamic viscosity, and cannot be smaller than the value of the dynamic viscosity at the launching altitude. In our case, the mass density and kinematic viscosity at the launching altitude are respectively around ~1 $kg.m^{-3}$ and 8×10^{-6} $m^2.s^{-1}$. This parameter is here to guarantee that the waves are ultimately dissipated over the few last model levels, if they have not been before (hence the division by the mass density at the altitude of launching ρ_0). This parameter was modified from 0.1 to 8×10^{-4} $kg.m^{-1}.s^{-1}$. This change is justified by the presence of several studies showing wave structures around 140 km altitude (Garcia et al., 2009), around 140–160 km (Kasprzak et al., 1993) at equatorial and intermediate latitudes as well as above 180 km altitude at polar latitudes (Persson, 2015), where GWs in Gilli et al. (2021) did not seem to propagate above 140 km. The saturation parameter controls the breaking of the GW by limiting the amplitude. A larger saturation parameter implies a larger saturating amplitudes. It must be of the order of 1 and was changed from 0.85 to 0.6. The probability distribution of the phase velocity amplitude was also modified. Previously, the phase velocity amplitude was chosen randomly between 1 and C_{max} (in $m.s^{-1}$). For the current version, the phase velocity amplitude is chosen randomly according to the Gaussian law centered on 0 with C_{max} as the standard deviation. The C_{max} value was kept fixed at 61 $m.s^{-1}$. Yet, to illustrate the implications of this change on the phase velocity, it can be noted that the mean absolute phase velocity amplitude is changed from 31 $m.s^{-1}$ to 48.7 $m.s^{-1}$. The horizontal wavelength range and the maximum value of the EP flux at the launching altitude (respectively 50–500 km and 0.005 $kg.m^{-1}.s^{-2}$) are not modified. These parameters are described in more details in Lott and Guez (2013).

Table 1
Baseline parameters used in the reference simulation. Values in the bracket indicate the interval range of distribution.

Phase velocity (Gaussian distribution) [$m.s^{-1}$]	Horizontal wavelength [km]	EP flux [$kg.m^{-1}.s^{-2}$]	Saturation	Diffusion [$kg.m^{-1}.s^{-1}$]
$\sigma = 61$	[50–500]	[0–0.005]	0.6	8×10^{-4}

2.2. Tuning of the upper-thermosphere

In contrast to the previous ground-to-thermosphere VGCM described in Gilli et al. (2021), the vertical extension presented here offers the opportunity to use the upper thermosphere data obtained by Pioneer Venus Orbiter to improve the simulation. A first comparison of the CO number density of the GCM version of Gilli et al. (2021) with the CO data obtained by Pioneer Venus Orbiter Neutral Mass Spectrometer (PV-ONMS; Niemann et al., 1980), showed that the CO number density at noon is smaller by a factor of 7–10 at 150 km altitude. The study of Gilli et al. (2021) was based on a collection of data mostly from Venus Express (2006–2014; low and middle solar cycle conditions; 80–150 s.f.u) experiments, and coordinated ground-based telescope campaigns in the upper mesosphere/lower thermosphere of Venus (80–150 km; listed in Gilli et al., 2021), and showed that GCM number density (for E10.7 = 140 s.f.u) of CO_2, CO and O, are comparable with observations in terms of trend and order of magnitude below 130–140 km altitude. The good agreement of the model with observations below 130 km and the discrepancy in CO and O number density above 130–140 km may suggest that the CO and O production rate are underestimated above 130–140 km.

In our simulations, the abundance of CO and O below 130 km altitude are not sensitive to the EUV flux, as the photochemical reaction rates are calculated for a fixed value of EUV solar radiation according to Atlas I solar spectrum reference (F10.7 = 192 s.f.u; Thuillier et al., 2004). As a result, the production of CO and O by photolysis of CO_2 is independent of EUV flux, which may lead to overestimate the density during the low and medium solar period. Another process to explore is ionospheric and neutral-ion chemistry which induce an additional production (and loss) term. Indeed, according to Brecht et al. (2011), where ion-neutral chemistry is based upon the chemical reactions and rates of Fox and Sung (2001), the oxygen production peak by the molecular oxygen ion dissociative recombination reaction ($O_2^+ + e^- \rightarrow O + O$) occurs around 140 km and oxygen production by neutral-ion and ion reaction becomes more important than the net photodissociation of CO_2 in the upper Venus thermosphere (Fox, 2007). O_2^+ and CO are produced by the following ion-neutral reactions:

$CO_2^+ + O \rightarrow O_2^+ + CO$

$O^+ + CO_2 \rightarrow O_2^+ + CO$

In the absence of ionospheric photochemistry in the IPSL VGCM, the photolysis of CO_2 into CO and O is the only contribution to CO and O production above 100 km and may explain the discrepancy in CO and O number density above 130 km. Moreover, chemical abundances play an important role in non-LTE effects (e.g., the impact of variable atomic O in the CO_2 cooling rates) and EUV heating processes, which are key processes in the upper atmosphere of terrestrial planets (Bougher et al., 1999). So, based on VEX/VIRTIS-H (Gilli et al., 2015) and PV-ONMS observations of CO, the rate of photolysis of CO_2 into CO and $O(^1D)$ above 135 km (~10^{-3} Pa at noon) was artificially increased (by a factor of 10) in this version of the IPSL VGCM to fit the observations. The need for this tuning raises interesting questions about the missing production of CO and O in the upper Venus thermosphere. However, this tuning is

more important by a factor at least 3 than what dissociative recombination can provide. Further developments will be needed to understand the lack of O and CO number density in the upper thermosphere. To explore this discrepancy in the composition, ionospheric chemistry is not the only possibility. Transport in this region is controlled by molecular diffusion (Müller-Wodarg et al., 2006), which is based in the IPSL VGCM (Gilli et al., 2017) on the algorithm developed by Chaufray et al. (2015). Investigating the sensitivity of the vertical composition profiles to this implementation will be done in future work, together with the implementation of ionospheric chemistry.

For the reference simulation, we used: 5×10^{-12} $cm^3.s^{-1}$ for the CO_2-O deactivation rate (in the brackets of experimental values: 1-6 $\times 10^{-12}$ $cm^3.s^{-1}$; see Gilli et al., 2017), 19.5% for the EUV heating efficiency and 200 s.f.u for the E10.7 solar flux index, corresponding to solar cycle 'high' flux values. In order to reproduce the averaged solar conditions of the data used, 4 reference E10.7 values were used: 135 s.f.u, 190 s.f.u, 200 s.f.u and 230 s.f.u. Due to a low number of observations and low geographic coverage above 260 s.f.u and below 120 s.f.u, it was chosen not to extend the simulations to these values.

3. IPSL VGCM model-data validation above 130 km and discussion

The results discussed in this section were obtained using simulations of the IPSL VGCM described in Section 2. The aim of this section is to present a comprehensive comparison of these simulations, focusing on the upper thermosphere (above 130 km altitude) with datasets from several missions: Pioneer Venus, Venus Express and Magellan. The altitude of the data was corrected to a common reference level (z = 0) corresponding to a radius of 6052 km above the centre of the planet. We took the distance to the centre of the planet of all observations ($R_i + z_i$), and subtracted it by the reference Venus radius. The instruments and measurements used in this validation are listed in Table 2. The geographical coverage (latitude, LT, SZA), altitude coverage and EUV conditions are also listed.

3.1. Upper thermosphere composition (He, N, CO, O, N_2, CO_2)

The most detailed observations of the neutral composition of the thermosphere above 140 km were made by the mass spectrometer (Neutral Mass Spectrometer; NMS) of Pioneer Venus Orbiter (PVO) between 1978 and 1980 during a period of high solar activity (~180–250 s.f.u; Niemann et al., 1980). This instrument measured, near the equator (centered on 16°N; 0°N-30°N), the thermospheric number densities of He, N, O, CO, N_2 and CO_2 covering nearly three diurnal cycles with an altitude range from 140–150 km to 250 km (300 km for He). For this study, the sensitivity factors (k-values) in Keating et al. (1985) are applied to the PV-ONMS measurements (x1.83 for the CO_2 and x1.58 for the others species). These factors were determined to make the PV-ONMS observations consistent with the PV-Orbiter Atmospheric Drag (OAD; Hedin et al., 1983; Keating et al., 1985) dataset. Pioneer Venus Orbiter did not make any direct observations of the exospheric temperature. Yet, from these species number density measurements and the density decay law, it was possible to reconstruct the temperature of the upper thermosphere around the equator ($|\text{latitude}| \leq 30°$) and for all local times (Niemann et al., 1980; Mahajan et al., 1990). A more detailed discussion about the exospheric temperature is provided in the next section.

Figs. 1 and 2 show the vertical profiles of the number density composition for several EUV conditions and on the dayside and nightside. The predicted atomic nitrogen number density is not modelled because the IPSL VGCM does not include nitrogen chemistry yet. Atomic oxygen becomes the dominant constituent above ~155 km altitude on the dayside and above ~145 km on the nightside according to the observations. Below these altitudes, CO_2 is the major constituent of the atmosphere. This evolution and these altitudes are well-reproduced by the IPSL VGCM. Both in the observed and modelled values, a small variation in the profiles can be seen in Fig. 1 when comparing lower and higher E10.7 indices. Our oxygen tuning seems to have reproduced well this sensitivity to EUV flux values. The O, CO, CO_2 and N_2 densities and variability are well reproduced by the IPSL VGCM. It should be noted that N_2 and CO are slightly overestimated by about 20% compared to the observations. Similarly to the dayside, the composition is well-estimated on the nightside (Fig. 2). The case of helium is interesting: On the dayside, the helium profile is rather well reproduced while on the nightside, the prediction is in the low range of the PV-ONMS observations. This is linked to an asymmetry in the number density profile of helium on the nightside, which is 4–5 times denser at 05 h than at 19 h (Niemann et al., 1980) for z = 167 km. This amplitude is not found with the IPSL VGCM, though there is an excess in the number density values of 50%.

A significant dispersion is visible on the density observations of the PV-ONMS, in particular on the nightside, which is partially reproduced by the IPSL VGCM. The origin of the dispersion of observation data may be here associated with the wave processes, as planetary waves and small-scale gravity waves which will more efficiently affect the density and temperature of the thermosphere (Kasprzak et al., 1993). These effects are weaker on the dayside because the atmosphere is more stable here. Given that the fields of the model are averaged over several Earth days, the dispersion linked to the wave processes of the IPSL VGCM is reduced, which explains why it is slightly underestimated.

Table 2
Observations of Temperature, Mass density, CO_2, CO, O and N_2 densities used in this paper. *: Here, for the E10.7 solar flux values, we adopted the Solar Irradiance Platform v2.37 solar flux model (SIP; formerly SOLAR2000; https://spacewx.com/sip/). The E10.7 solar flux index is adjusted for the Earth-Sun-Venus angle but remains standardised to 1 AU. Here, the reference Venus radius is 6052 km.

Instrument/Experiment	Method	Lat coverage	LT coverage	EUV coverage (E10.7)*	Altitude coverage	(Retrieved) variable	References
Magellan	Aerobraking	10–16°N	10–18H	110–140 s.f.u	135–150 km	Mass density	Giorgini et al., 1995; Tolson et al., 2013
Magellan	Precise Orbit Determination	10–16°N	0–24H	120–160 s.f.u	170–185 km	Mass density	Tolson et al., 2013
Pioneer Venus Orbiter	Precise Orbit Determination	~16°N	0–24H	180–280 s.f.u 180–260 s.f.u	150–240 km 150–190 km	Mass density	Tolson et al., 2013 Keating et al., 1980
Pioneer Venus Orbiter Neutral Mass Gas Spectrometer	Neutral Mass Gas	10–30°N	0–24H	180–260 s.f.u	150–250 km	Composition, Number Density, (temperature)	Niemann et al., 1980: Joy, 2012; Kniffin, 1993
Venus Express/VExADE-AER	Aerobraking	70–90°N	4.4–6.3H	110–150 s.f.u	130–150 km	Mass density	Müller-Wodarg et al., 2016
Venus Express/VExADE-TRQ	Torque measurements	70–90 °N	78–98° SZA	100–160 s.f.u	160–200 km	Mass density	Persson, 2015
Venus Express/VExADE-POD	Precise Orbit Determination	80–90°N	Terminator	90–160 s.f.u	160–190 km	Mass density	Rosenblatt et al., 2012

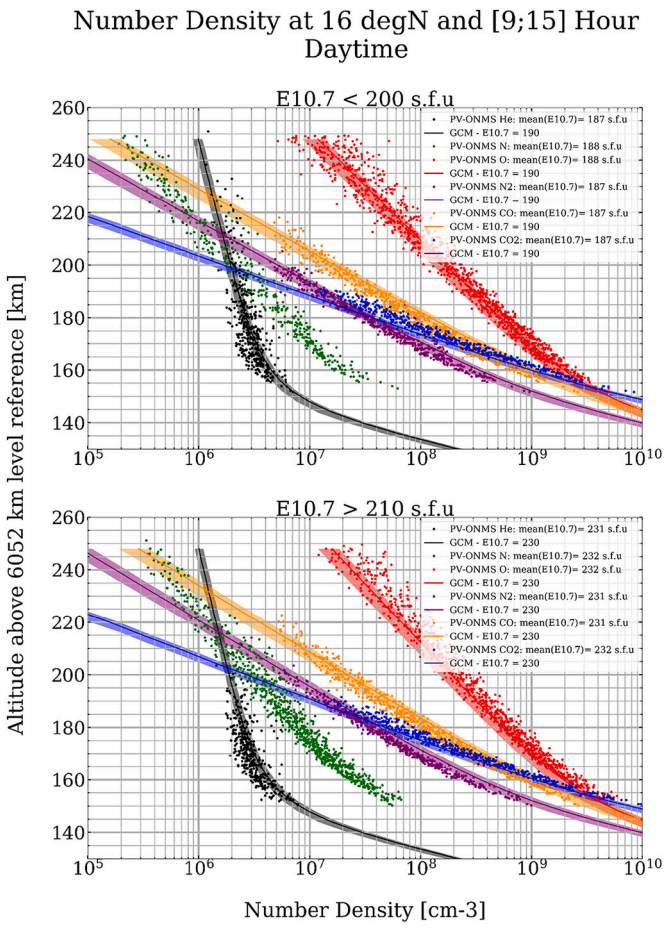

Fig. 1. Vertical profiles of the upper thermosphere number density composition (O: red; CO: orange; CO_2: blue; N_2: purple, N: green; He: black) for several E10.7 (top: E10.7 < 200 s.f.u; bottom: E10.7 > 210 s.f.u) conditions between 9 and 15 h local solar time. The points correspond to the PV-ONMS observations. The lines correspond to the densities predicted by the IPSL VGCM. The coloured areas correspond to the min/max variability of the corresponding number density. The modelled densities are not plotted above 250 km because the top of the model is close to this altitude. The predicted atomic nitrogen number density is missing because the nitrogen chemistry is not yet included in this model. (For interpretation of the references to colour in this figure legend, the reader is referred to the web version of this article.)

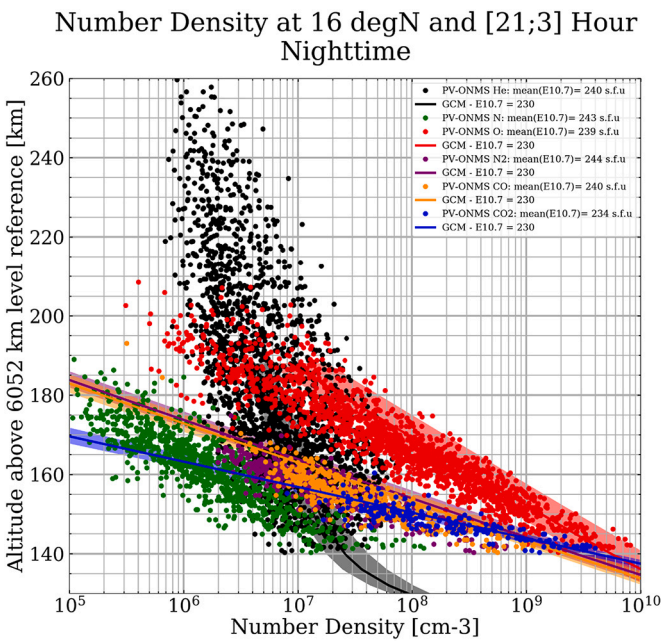

Fig. 2. Vertical profiles of the upper thermosphere number density composition (O: red; CO: orange; CO_2: blue; N_2: purple, N: green; He: black) between 21 and 03 h local solar time. The points correspond to the PV-ONMS observations. The lines correspond to the densities predicted by the IPSL VGCM. The coloured areas correspond to the min/max variability of the corresponding number density. The modelled densities are not plotted above 190 km because the top of the model is close to this altitude. The predicted atomic nitrogen number density is missing because the nitrogen chemistry is not yet included in this model. (For interpretation of the references to colour in this figure legend, the reader is referred to the web version of this article.)

3.2. Exospheric temperature

The major neutral species in the PV-ONMS measurement region is atomic oxygen. Kinetic temperatures were derived here from that dataset assuming hydrostatic equilibrium and fitting the PV-ONMS atomic oxygen data to $N(z) = N(z_0) \bullet e^{\frac{-(z-z_0)}{H}}$ where $H = \frac{k_B \bullet Texo}{m_0 \bullet g(z)}$ is the scale height. Z is the altitude, z_0 is the reference altitude (depends on the orbit), N(z) is the number density at z, k_B is the Boltzmann constant, g(z) is the gravitational acceleration with g(0) = 8.87 $m.s^{-2}$, T_{exo} is the exospheric value of the temperature (which is constant from the middle thermosphere upward) and m_0 is the molar mass (here 16 amu for the atomic oxygen). The O data used in the determination of the scale height H were representative sample averages at 12 s time intervals. The scale heights were determined in this work by following the method and updated constraints described in Mahajan et al. (1990) to select and fit the atomic oxygen data. Typically, only data above 170 km on the day side and 150 km on the night side were used to minimise the effects of the temperature gradient. Orbits retained include at least 5 points and an altitude range larger than 20 km. Finally, fits where the absolute value of the correlation coefficient was below 0.9 were excluded. This operation allowed us to reconstruct the exospheric temperature from O number density on nearly three diurnal cycles, covering an E10.7 EUV index range from 180 to 260 s.f.u, around the equator.

Fig. 3 shows the diurnal variation of the Venusian exospheric temperature derived from the atomic oxygen height scale around E10.7 = 200 ± 15 s.f.u (from 185 to 215 s.f.u). The nightside temperature is 116

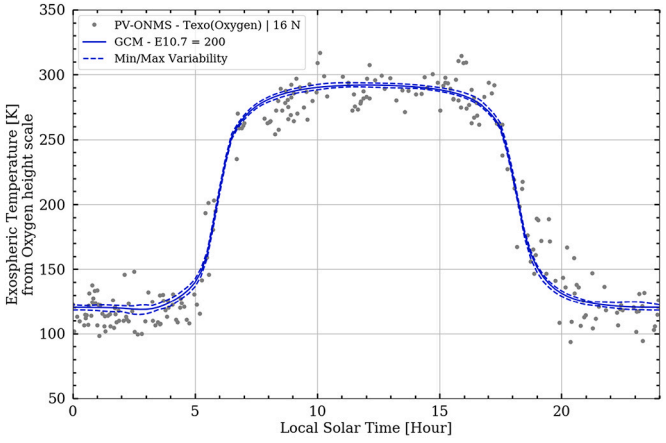

Fig. 3. Diurnal variation of the Venusian exospheric temperature derived from the oxygen height scale (grey points) and predicted by the IPSL VGCM (blue) at 16° North for E10.7 = 200 ± 15 s.f.u. The exospheric temperature is averaged between 10^{-6} Pa and 10^{-8} Pa for the GCM. The Min/Max variability corresponds to the minimum and maximum values of the modelled temperature in the pressure range and latitude of interest. The gap between 6 and 7.5 h LT is due to the lack of data respecting the restricting conditions. (For interpretation of the references to colour in this figure legend, the reader is referred to the web version of this article.)

± 11 K ("cryosphere") while the dayside temperature is 287 ± 11 K according to the PV-ONMS data at 200 ± 15 s.f.u, with a rapid hourly evolution at 6 and 18 h LT. The diurnal variation of the exospheric temperature predicted by the IPSL VGCM is in excellent agreement with the retrieved exospheric temperature with 291 ± 2 K around noon and 120 ± 4 K around midnight which is also consistent with Niemann et al. (1980).

On the dayside, The IPSL VGCM variability of the exospheric temperature is of the order of 2 K, which is less than the one of the reconstructed exospheric temperatures. This difference can be partially explained by three reasons. The first one is the effect of the temperature gradient on the number density with altitude, which we have tried to minimise but which may underestimate the temperature. The second is that the observations are chosen with an EUV flux between 185 and 215 s.f.u. The reconstructed temperature for 190 s.f.u. will generally be lower than that for 210 s.f.u. If we refer to the dependence of the temperature with E10.7 index, given in Fig. 4 (the linear rate coefficient a), this range of E10.7 values would give us a variability between 5 and 9 K around 285-290 K. The last reason is the period during which each time step of the fields is averaged (~5 Earth days for a total of 24 steps per Venusian day). This period is long enough to affect the variability due to waves (small-scale gravity waves and planetary-scale waves) and will therefore reduce the apparent variability of the model. This effect is especially visible on the nightside where wave activity is stronger as seen in Figs. 2, 4 and 5. In Fig. 3, observed variability is stronger near the evening terminator than on the morning side. This feature is not reproduced by the model.

Fig. 4 shows the response of the nightside (top) and dayside (bottom) exospheric temperature to the solar activity variations. The temperature dispersion for a constant E10.7 index is mainly related to internal sources such as planetary or small scales gravity waves whose effects are much more important on the night side than on the day side as can be seen in Fig. 2. The variability of E10.7 is here mainly due to the rotation of the sun (short-term solar activity) during the high solar activity period, which is 28.6 days from Venus orbit. A linear regression of the exospheric temperature with the E10.7 values between 9 and 15 h LT (N = 84 which N is the number of measurements respecting the LT conditions) gives a slope of ~0.48 K/s.f.u. Note that reducing this interval to

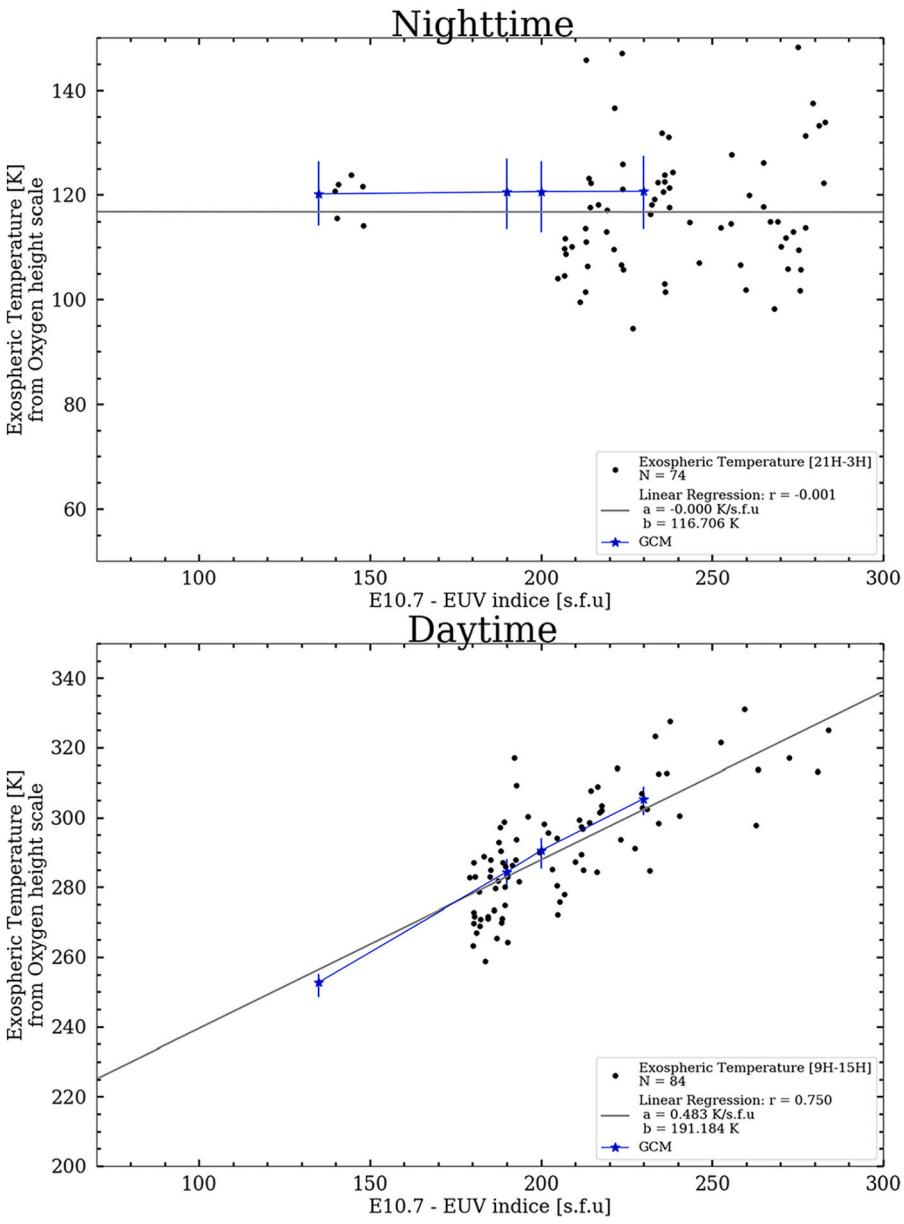

Fig. 4. Dependence of exospheric temperature with E10.7 solar flux index. The black points correspond to the retrieved exospheric temperatures from PV-ONMS oxygen number density observations between (bottom) 09-15 h LT and between (top) 21-03 h LT. The grey line corresponds to the linear regression of the retrieved exospheric temperatures with the E10.7 solar flux index. The blue line and markers correspond to the exospheric temperatures predicted by IPSL VGCM for several E10.7 values. The vertical lines correspond to the min/max variability. The values around 140 s.f.u correspond to the few PV-ONMS observations made in 1991 during the intermediate solar activity. The E10.7 solar flux index is adjusted for the Earth-Sun-Venus angle but remains standardised to 1 astronomic unit. (For interpretation of the references to colour in this figure legend, the reader is referred to the web version of this article.)

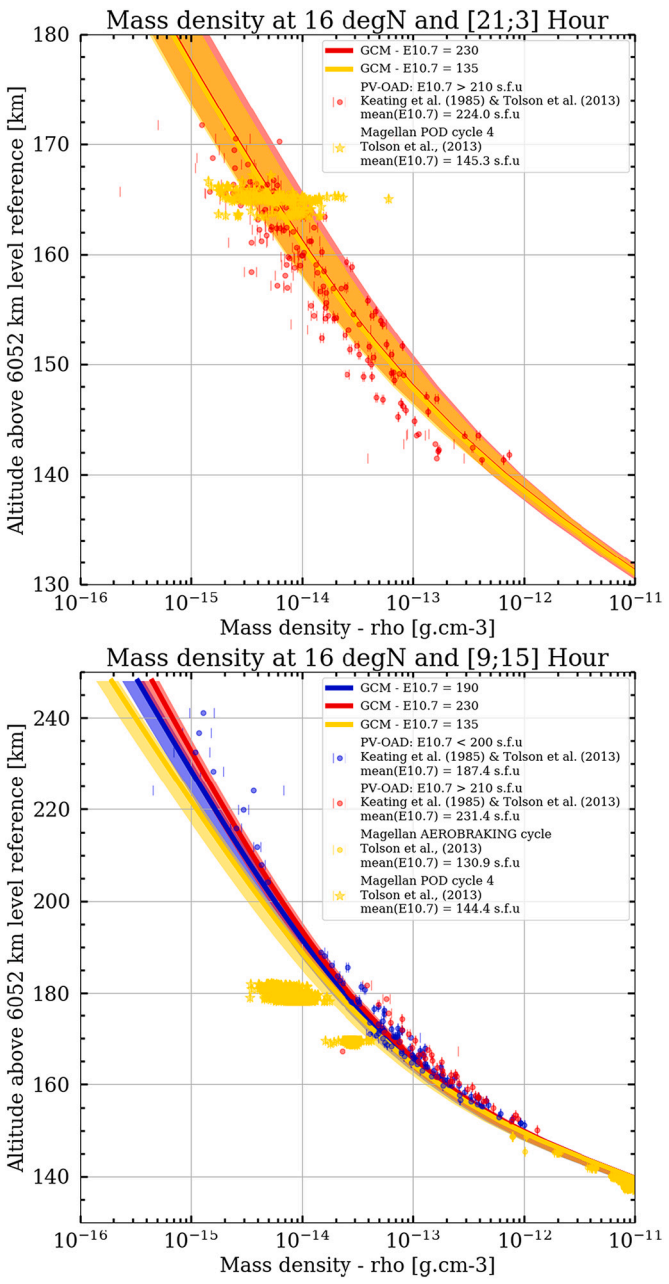

Fig. 5. Vertical profile of the mass density between 9 and 15 h LT (bottom) and between 21 and 03 h LT (top). The blue points correspond to the PV-OAD measurements for E10.7 < 200 s.f.u, the red points correspond to the PV-OAD measurements for E10.7 > 210 s.f.u and the yellow point correspond to the Magellan measurements (120–160 s.f.u). The IPSL VGCM predicted profiles are plotted with solid lines. The E10.7 solar flux index is adjusted for the Earth-Sun-Venus angle but remains standardised to 1 AU. (For interpretation of the references to colour in this figure legend, the reader is referred to the web version of this article.)

10-14 h LT ($N = 49$) gives a slope of ~0.43 K/s.f.u, and ~ 0.58 K/s.f.u for 10.5–13.5 h LT ($N = 37$). This illustrates the range of uncertainty for the dataset on the evolution of the temperature in the short-term EUV variations. Due to the lack of data to reconstruct the exospheric temperature at the equator during low and average solar activity, it is only possible, for future developments, to extrapolate this sensitivity for values below 170 s.f.u to estimate the temperature during the Venus Express or Magellan activity period.

On the dayside, the IPSL VGCM sensitivity is around ~0.555 K/s.f.u between 190 and 230 s.f.u. This slope is slightly high compared to the slope estimated via linear regression but it remains within the uncertainties as discussed above. Keating et al. (1985) and Hedin et al. (1983) give a sensitivity of 0.40–0.43 K/s.f.u while Mahajan et al. (1990) indicate a sensitivity of 0.5–0.6 K/s.f.u with the same PV-ONMS data. These differences may be due to several elements: the use of E10.7 instead of F10.7 which modifies the EUV flux distribution as explained in Section 2, the difference in constraints on the PV-ONMS data to obtain the exospheric temperature and the correction of the Earth-Sun-Venus angle for the calculation of the daily-averaged E10.7. Indeed, the correction of the Sun-Venus-Earth angle allows to estimate, from the observations on Earth at a time t, the value of E10.7 at a time t + dt or t-dt. It allows to reproduce well the solar rotation cycle, but it does not completely take into account the solar flare events which punctually increase the EUV flux and thus the temperature of the exosphere as shown by the event of September 10, 2017 on Mars (Fang et al., 2018). Depending on whether these events occur towards Earth or Venus, they may cause a slight underestimation or overestimation of the E10.7 for Venus.

On the nightside, the PV-ONMS data seem to show no (or very weak) dependence between exospheric temperature and EUV flux for our EUV range (high solar activity). Moreover, Piccialli et al. (2015) published the vertical temperature profile on the nightside between 90 and 140 km with VEX/SPICAV from stellar occultation and found 120 ± 10 K at 140 km around midnight during the medium solar activity period (100–140 s.f.u), which is similar to the temperature retrieved from Pioneer Venus data at high solar activity period and the one predicted by the IPSL VGCM. This trend is well reproduced by the model. Keating and Hsu (1993) have updated the VIRA model in order to study the influence of the long-term EUV variations on the exospheric temperature and found a sensitivity of 30–35 K for 50 s.f.u (from 130 to 180 s.f.u), so ~0.6–0.7 K/s.f.u at noon, and a sensitivity lower than 0.15–0.2 K/s.f.u at midnight. In Keating and Bougher (1992), they also studied the sensitivity of the exospheric temperature with the short-term EUV variations and gave an EUV heating efficiency value range of 16–23% and an O-CO_2 cooling coefficient range of 1-4 × 10^{-12} cm^3 s^{-1} where the observed response of temperature to short-term solar variability could be reproduced by their atmospheric model. Fox (1988) suggests EUV heating efficiency between 20 and 25% with a high O-CO_2 cooling effect (≥1 × 10^{-12} cm^3 s^{-1}). Our current values are respectively 19.5% and 5 × 10^{-12} cm^3 s^{-1}, which are consistent with these studies.

3.3. Mass density

The thermospheric density is too low to make direct measurements with remote sensing instruments. In order to retrieve the thermospheric density, three methods are here used, related to the aerobraking technique for orbit modification: The Precise Orbit Determination (POD), the torque and the accelerometry (Persson, 2015). The last method is used in the range ~ 130–150 km altitude and consists in measuring the acceleration, by the on-board accelerometers, experienced by the spacecraft due to the flux of molecules impacting on its surface (Müller-Wodarg et al., 2016) and, from these measurements, the mass density is estimated. Yet the mass density needs to be sufficiently high in order to return a measurable signal. The two first methods are used for altitudes where the accelerometry cannot be used. They use the friction caused by passage through the planetary atmosphere, which provides a velocity change at periapsis or induces a torque between the solar panels, in order to estimate the mass density (Keating et al., 1985; Giorgini et al., 1995; Persson, 2015). Here these three types of data are used to make a comparison of the observed upper thermosphere with the modelled mass density distribution.

3.3.1. Equator

Pioneer Venus Orbiter and Magellan spacecrafts carried out several aerobraking campaigns around the equator. Since these campaigns occurred during different solar cycle conditions (PVO: 180–250 s.f.u;

VEX & Magellan: 100–150 s.f.u, see Table 2), these datasets allow us to study the evolution of the mass density with the solar activity. Fig. 5 shows a comparison between the mass density determined from Magellan and Pioneer Venus Orbiter spacecraft at equatorial latitudes (0°-30°) centered on 16°N and the IPSL VGCM mass density predicted profile for different E10.7 solar flux value (yellow line: E10.7 = 135 s.f.u; red line: E10.7 = 230 s.f.u; blue line: E10.7 = 190 s.f.u). The mass density value and decay predicted by the IPSL VGCM is consistent with the observations in the 190 and 230 s.f.u cases, even though there is a slight shift in the amplitude of the decay from 150 km altitude. Mainly in the dayside region, the variability of the Magellan POD cycle 4 measurements is larger than the variability of the PV-OAD measurements. This can be partly explained by the fact that the uncertainty of the Magellan POD cycle 4 measurements is of the order of magnitude of the observations, which is also larger than the uncertainty of the PV-OAD measurements. Another possibility is an uncertainty in the altitude determination. Indeed, Tolson et al. (2013) suggest that the relative orbit determination errors of the cycle 4 are significant on the nightside and on the afternoon.

For the E10.7 = 135 s.f.u case, the IPSL VGCM over-estimate the mass density by a factor two compared with Magellan POD cycle 4 observations (above 160 km altitude). This can be explained by the fact that photolysis rates are computed for high solar activity (see Section 2.2) while the Magellan observations were made during the medium solar activity. This implies that the CO and O modelled productions are higher than what should be for E10.7 = 135 s.f.u and, here, only the temperature profile above 140 km will change due to the variation of the EUV flux in our model. Therefore, if our model is able to reproduce the correct number density structure between 190 and 230 s.f.u, it will overestimate the oxygen number density compared with the observations during the intermediate solar conditions. This confirms that the evolution of oxygen production with solar activity has an important role in the physics of the thermosphere. According to Keating and Hsu (1993), the oxygen number density at 150 km should be 20–25% lower at F10.7 = 130 s.f.u than at F10.7 = 180 s.f.u.

The nightside mass density predicted by the IPSL VGCM does not seem to be affected by solar activity which seems consistent with the comparison between PV-OAD and Magellan POD cycle 4 data. However, Tolson et al. (2013) point out that the mass density values of the cycle 4 have a large uncertainty due to errors altitude determination. Moreover, because the nightside oxygen is produced on the dayside, Keating and Hsu (1993) suggest that the oxygen production is lower during the minimum and medium solar activity than the maximum solar activity and the reduced production on the dayside due to the decreased solar activity should cause reduced nightside density.

Fig. 6 shows a comparison of the local time evolution (top) and the vertical profile (bottom) of the mass density measured during the Magellan Aerobraking campaign (Giorgini et al., 1995) with that predicted by the IPSL VGCM along the Magellan trajectory. The IPSL VGCM (yellow points) seems to overestimate the mass density between 150 and 130 km altitude by 30 to 70% depending on local time, although it reproduces its evolution. The indigo curve represents the mass density predicted by the model, but 1.8 km higher than the altitude of Magellan (corresponds to 0.4–0.6 scale height for the altitude range 130–150 km), and it shows better agreement with the Magellan data. On the dayside, at 135 km, the major species is CO_2 at >80%, the other species such as O and CO have little influence on the mass density, and our model therefore has a slight altitude shift that can be explained by a slightly different thermal profile between 110 and 150 km altitude. Constraining the daytime temperature profile between 110 and 150 km altitude is a complex exercise, as shown by Gilli et al. (2021) because of the temperature uncertainty of the order of 20 to 60 K in the available dataset (retrieved from Venus Express/VIRTIS-H non-LTE emissions, Gilli et al., 2015).

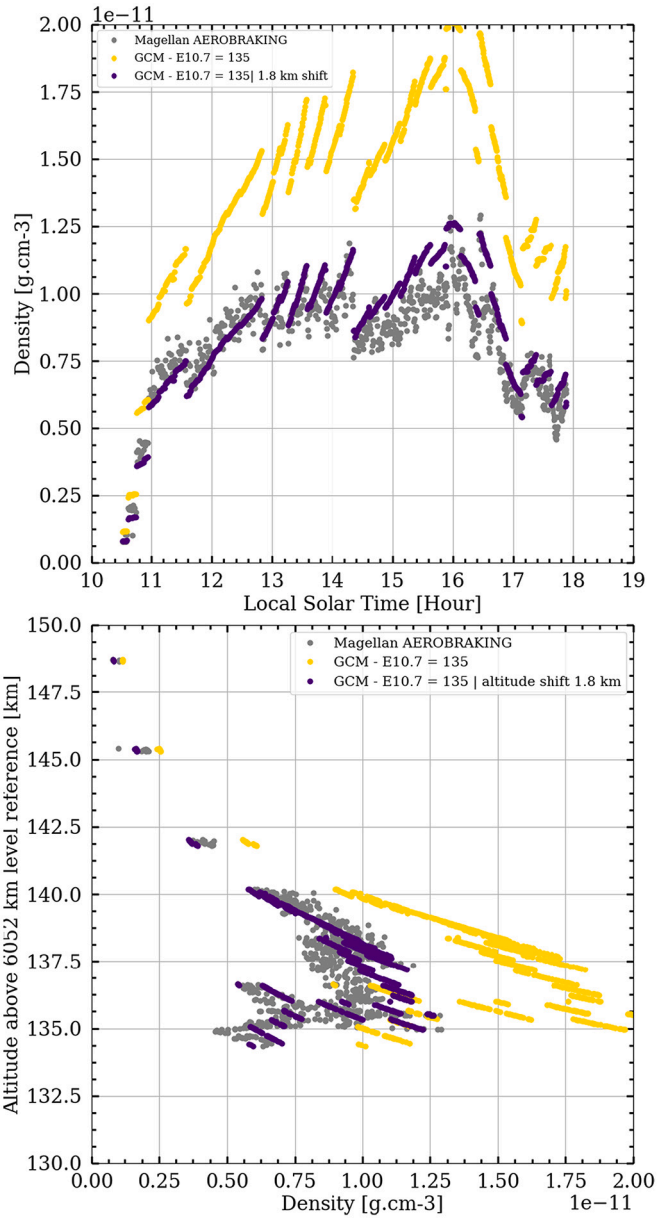

Fig. 6. Comparison of the local time evolution (top) and the vertical profile (bottom) of the mass density measured during the Magellan aerobraking campaign (Giorgini et al., 1995) with that predicted by the IPSL VGCM along the Magellan trajectory. The grey points correspond to the Magellan data. The IPSL VGCM predicted values are plotted with yellow points. The indigo points correspond to the mass density predicted by the model but for an altitude 1.8 km higher. (For interpretation of the references to colour in this figure legend, the reader is referred to the web version of this article.)

3.3.2. Northern pole

Fig. 7 shows the vertical profiles of the mass density measured during the VExADE campaigns at the morning (bottom) and evening (top) terminator at high latitudes (70°N-90°N) during intermediate solar activity (~135 s.f.u). The predicted mass density of the Venusian thermosphere at high latitudes is consistent with the Venus Express observation. There seems to be a slight asymmetry in the mass density between morning (slightly less dense) and evening (slightly denser), which is observed by the data. Yet, as seen with the Magellan data at the equator, the modelled mass density is over-estimated in contrast to the observations. The largest discrepancies are seen above 160 km altitude, i.e. towards the altitude where atomic oxygen exceeds CO_2. These

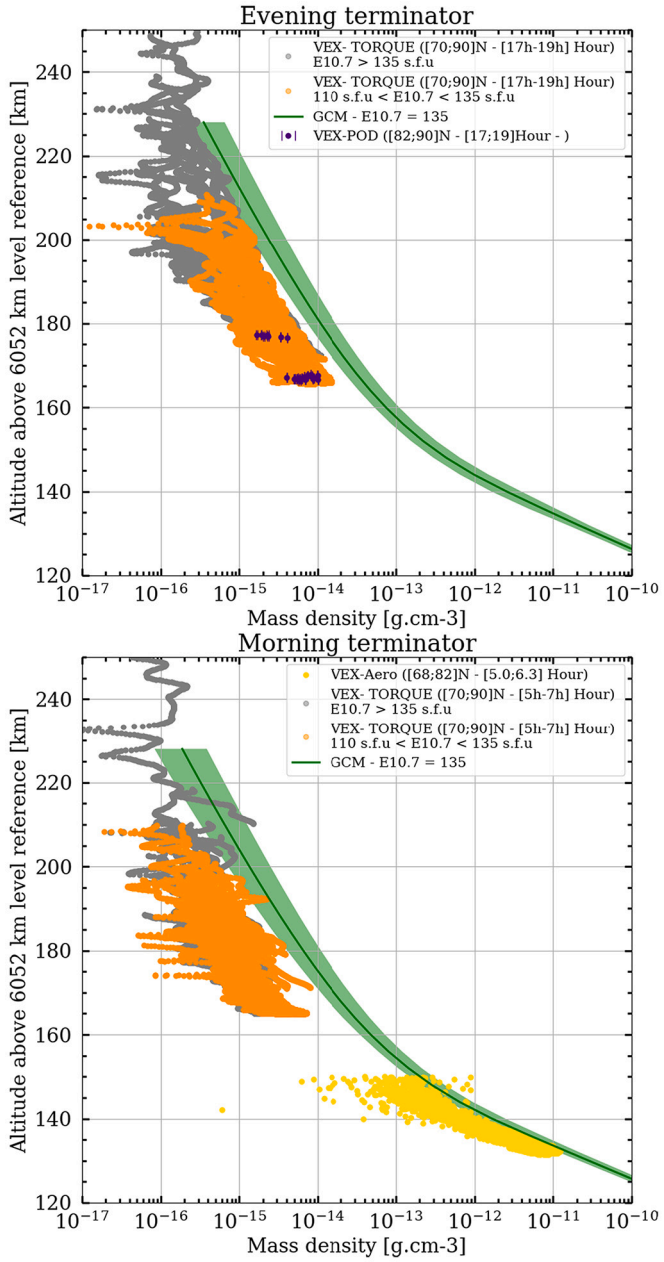

Fig. 7. Vertical profile of the mass density near the terminator (bottom: 5-7 h LT; top: 17-19 h LT) at high latitudes (70°N-90°N). The purple points correspond to the VEX POD measurements (Rosenblatt et al., 2012), the grey and orange points correspond to the VEX Torque measurements (Persson, 2015) and the yellow points correspond to the VEX aerobraking measurements (Müller-Wodarg et al., 2016) for different EUV solar flux conditions. The IPSL VGCM predicted profiles are plotted with solid green line. The modelled mass density is not plotted above 230 km because the top of the model is close to this altitude. The E10.7 solar flux index is adjusted for the Earth-Sun-Venus angle but remains standardised to 1 AU. (For interpretation of the references to colour in this figure legend, the reader is referred to the web version of this article.)

discrepancies could be related to the thermal profile and oxygen production that is adjusted for high solar activity.

4. Discussion

4.1. Impact of non-orographic GW

There is little observational data of gravity wave structures over long periods, although Garcia et al., (2009) report the presence of wave structures between 115 and 140 km altitude, between 130 and 170 km altitude at equatorial latitude (Kasprzak et al., 1993) and even above 160–180 km altitude at polar latitudes in Persson (2015). This makes the parameterization of non-orographic gravity waves in the upper thermosphere difficult. A complete analysis of the wind and number density distributions driven by gravity waves is outside the scope of this work, but some effects of the new parameterization and tuning are highlighted here.

Figs. 8, 9 and 10 show the impact of our parameterization of non-orographic gravity waves (see Section 2.1) on the zonal wind distribution, the diurnal variation of the temperature averaged between 10^{-6}–10^{-8} Pa and the He abundance distribution map at $p = 10^{-6}$ Pa predicted by the IPSL VGCM. The tuneable GW parameters used here are listed in Table 1 and described in Section 2.1. Fig. 8 shows the westward zonal wind field (local time versus altitude) modelled with the GW parameterization of Gilli et al. (2021) (top) and the new GW parameterization (bottom). The non-orographic gravity waves drag (contours) level reference are in 10^{-6} m.s^{-2} and 10^{-4} m.s^{-2} at top and bottom respectively. In contrast to the paper by Gilli et al. (2021), the top simulation does not show wind asymmetry and the winds are higher by a factor of 1.5–2. (Fig. 8, top part). This is due to changes in the non-LTE CO_2 near infrared heating rate (see Fig. A.1 in Appendix A) which has influenced the distribution of the winds between 90 and 150 km altitude and made the propagation of the gravity waves less efficient, especially on the evening side. The increase in the saturation factor and the decrease in the dissipation factor (see Section 2.1) allowed the propagation of gravity waves at higher altitudes and with greater amplitude. Through momentum deposition, the waves slow down the winds at higher altitudes. The GW drag peak is located for this study at 140–160 km altitude compared to 120–130 km in Gilli et al. (2021). Another effect shown in Fig. 8 (bottom) is an asymmetry of the SS-AS zonal flow between the morning and evening side and at altitudes above 100 km with the current GW parameterization, due to asymmetry in the GW propagation.

Fig. 9 shows the helium concentration map at p = 10^{-6} Pa before (top) and after (bottom) our new GW parameterization. It can be seen that the improved parameterization has changed the nightside distribution of helium. With the previous GW parameterization, the IPSL-VGCM does not show an asymmetry in the helium number density with the local time and the number density is maximum at midnight. In the case of our current parameterization, if the maximum at midnight does not disappear completely, an over-density of helium appears around 4-5 h LT compared to the evening. Niemann et al. (1980) found an asymmetry of helium number density on the night side at the same local times from PV-ONMS data at 157 and 167 km with a number density 4–5 times higher on the morning side than on the evening side. This amplitude is not found with our simulations, even though there is an overdensity of 50% compared to the evening.

This underestimation of the asymmetry could come from several points: first, it could mean that the current parameterization is too weak to induce such a contrast. However, heavier species such as N_2 also show a slight asymmetry (not shown), which is not confirmed by the observations. It is therefore likely that the waves are a component of the solution without being the main one. The second hypothesis is related to the large-scale circulation and to the presence of an accumulation of matter around midnight. This is related to the associated descent of air near midnight may prevent the asymmetry to build up.

The reduction of the nightside temperature compared to Gilli et al. (2017) comes here mainly from changes in non-orographic gravity waves parameterization. Indeed, the current CO_2-O cooling did not allow the temperature to cool below 140 K at midnight with the GW parameterization of Gilli et al. (2017, 2021). Fig. 10 shows the diurnal variation of the temperature averaged between 10^{-6} Pa and 10^{-8} Pa for two GW configurations of the current IPSL VGCM. In blue, our current GW parameters presented in Section 2 and in red the same GW

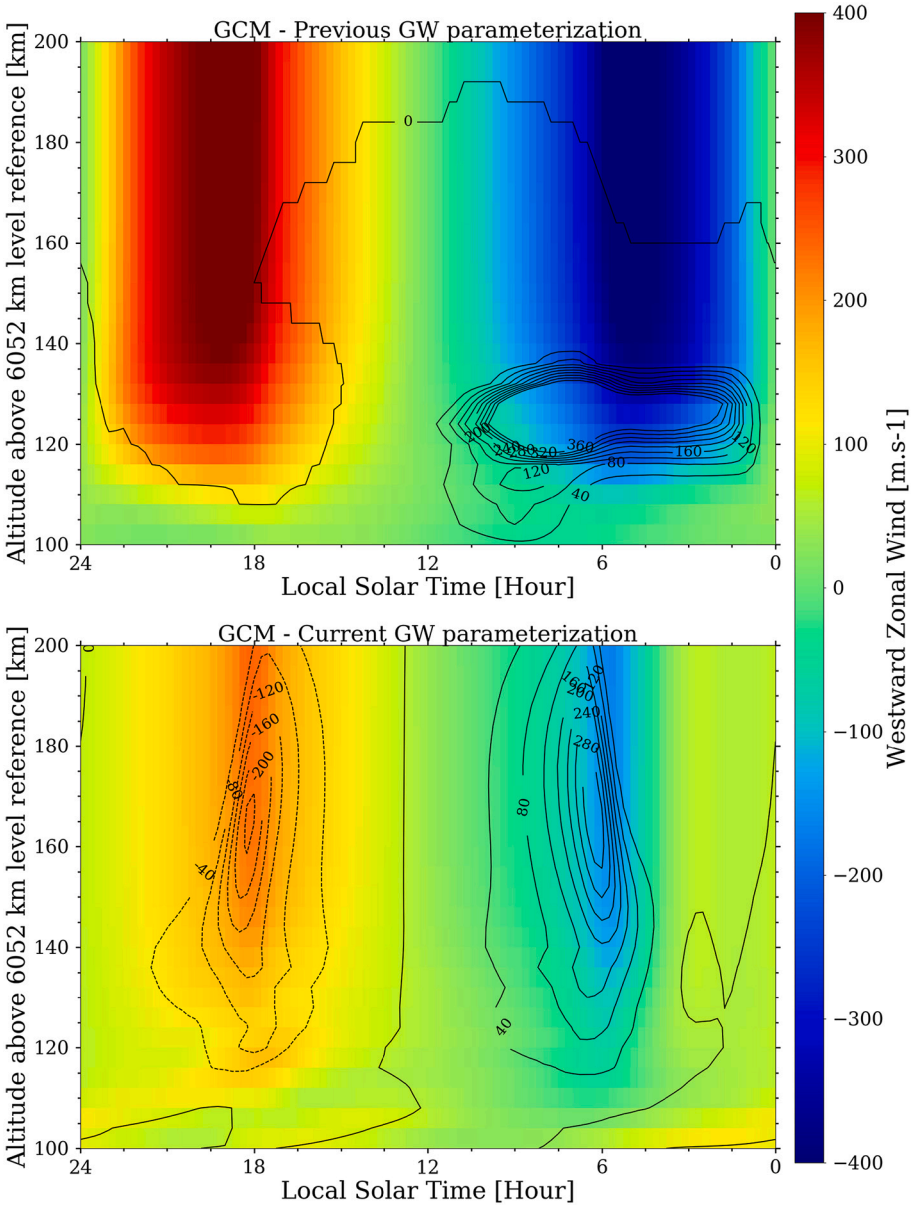

Fig. 8. Local time vs altitude map of the westward zonal wind and non-orographic gravity waves drag (contours) averaged for latitudes 20°S-20°N for (top) previous and (bottom) current GW parameterization. Solid black line indicates acceleration by GW drag, dashed black line deceleration. The GW drag level references are in 10^{-6} m.s^{-2} and 10^{-4} m.s^{-2} at top and bottom respectively.

parameters used in Gilli et al. (2021). It can be seen that the change in GW parameters had a small effect on the daytime temperature profile, but that the temperature decreases by over 20–40 K at midnight. Increasing the altitude where the waves break and their amplitude may have enhanced the slowing of the day-to-night transport, which transports matter and transfers heat from day to night.

4.2. Composition

As seen in Figs. 1 and 2, the IPSL VGCM number density dayside and nightside profiles show good agreement with the PV-ONMS observations during high solar activity. To achieve this result, the photolysis of CO_2 to $O(^1D)$ was increased tenfold above 135 km altitude, to compensate the lack of oxygen in this altitude range in standard simulations. Dissociative recombination of O_2^+ as well as ionospheric chemistry can provide an additional source of atomic oxygen above 130 km altitude, becoming even more important than the photodissociation of CO_2 (Brecht et al., 2011). However, this additional production would remain several times lower than a factor of 10 and cannot therefore explain the lack of atomic oxygen and CO in the thermosphere. Moreover, the fact that CO and N_2 are 30–50% denser than observed suggests that molecular diffusion and transport processes should also be investigated. Future developments will be addressed to take into account the ionospheric chemistry, explore the sensitivity to molecular diffusion, or find another oxygen production source in order to fix the thermospheric number density question.

5. Conclusion

The GCM used here is an improved and extended version of the model described in Gilli et al. (2017, 2021). Improvements have been made on the parameterization of non-LTE CO_2 near infrared heating and on the parameterization of non-orographic gravity waves. To reproduce O and CO number densities in the thermosphere, a tuning was done by increasing significantly the photodissociation of CO_2 into CO and O for altitudes above 135 km. The validation was performed using

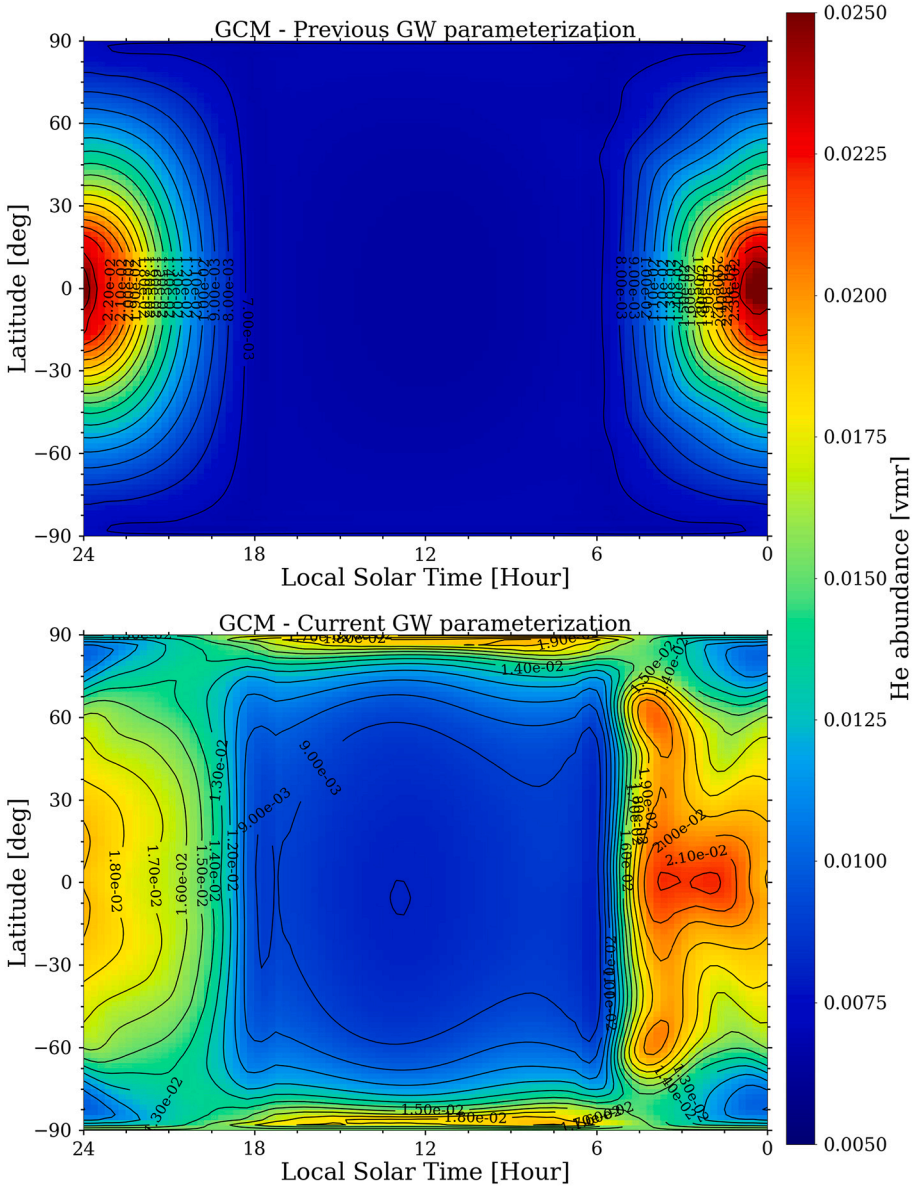

Fig. 9. Local time-latitude cross sections of longitudinally averaged helium abundance field over two Venusian days at p = 10^{-6} Pa. They correspond to previous (top) and current (bottom) GW parameterizations.

temperature, number densities and mass density data from the Pioneer Venus, Magellan and Venus Express missions.

Despite the initial underestimation of the atomic oxygen number density above 130–140 km by a factor of 10, the increase by the same factor of the CO_2 photodissociation into O and CO above these altitudes range allow to fit very well the vertical profile of the PV-ONMS number density and to reproduce the temperature and density evolution of the Venusian thermosphere during high solar activity (180–230 s.f.u). At equatorial latitude, the exospheric temperature, as well as its sensitivity to solar activity, around ~0.555 K/s.f.u predicted by the IPSL VGCM, is close to that reconstructed from the PV-ONMS oxygen number density data during the high solar activity period. Based on available data, the nightside exospheric temperature does not seem to be influenced by the EUV index and remains around 116 K for the observations and 120 K for the model. The reduction of the nightside temperature compared to Gilli et al. (2017) comes mainly from changes in the non-orographic gravity wave parameterization. Our results suggest that the increase of their amplitude and the altitude where the waves break (above 130 km) have weakened the day-to-night transport. The difficulty in tuning the GW parameterization comes from the lack of systematic GW observations which are necessary to constrain the model parameters. However, observations of wave structure at 140 km altitude and above 160–200 km altitude at the poles led us to parameterize our GWs so that they propagate above 140 km.

Significant data-model discrepancies are still to be noted. Without our tuning on CO_2 photodissociation, both O and CO are underestimated by a factor 7–10 above 135 km. This needed tuning shows that the IPSL VGCM, which only takes into account neutral photochemistry, is missing an important oxygen and CO production term. This emphasizes the need to include ionisation and ionospheric chemistry, which should be a priority in the evolution of the IPSL VGCM, together with an investigation of the sensitivity to molecular diffusion parameterization. Secondly, the mass density is overestimated by at least a factor 1.5–3 for altitudes above 160 km and for E10.7 = 135 s.f.u. This overestimation is directly related to the absence of evolution due to E10.7 in the neutral photochemistry which is adapted for high solar activity. This dependency will need to be studied in the future to be added to the IPSL VGCM and adjusted to the observations.

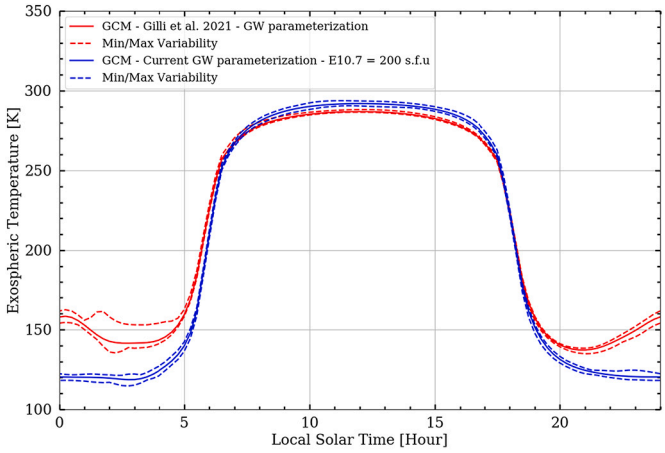

Fig. 10. Diurnal variation of the Venusian exospheric temperature predicted by the IPSL VGCM at 16° North for E10.7 = 200 s.f.u for several GW parameterizations. The GW parameters used in Gilli et al. (2021) and in this study are respectively plotted in red and blue solid lines. The exospheric temperature is averaged between 10^{-6} Pa and 10^{-8} Pa for the GCM. The Min/Max variability corresponds to the minimum and maximum values of the modelled temperature. (For interpretation of the references to colour in this figure legend, the reader is referred to the web version of this article.)

Declaration of Competing Interest

None.

Data availability

No data was used for the research described in the article.

Acknowledgements

The "PVO-V-ONMS-4-NEUTRALDENSITY-12SEC-V1.0" and "PVO-V-POS-5–VSOCOORDS-12SEC-V1.0" are obtained from the Planetary Data System (PDS) (https://pds.nasa.gov/). The authors thank Robert H. Tolson for providing Magellan aerobraking and PV-OAD data, Moa Persson, Ingo Müller-Wodarg and Pascal Rosenblatt for providing the Venus Express VExADE datasets, as well as François Lott for his advices on the GW parameterization. This work was funded by ESA under the contract No. 4000130261/20/NL/CRS. The IPSL VGCM simulations were done thanks to the High-Performance Computing (HPC) resources of Centre Informatique National de l'Enseignement Supérieur (CINES) under the allocation n°A0100110391 made by Grand Equipement National de Calcul Intensif (GENCI).

Appendix A

The model includes parametric equations that mimics the heating rate calculated by line by line non-LTE simulation (Roldan et al., 2000) for each pressure level p and solar zenith angle χ.

$$\frac{\partial T_i}{\partial t}(p,\mu) = \frac{\partial T}{\partial t}\left(p_{0,i}, \mathrm{r}_0, 1\right) \times \left(\frac{p_{0,i}}{p}\right)^{a_i} \times \widetilde{\mu}^{m_i} \times \left(1 + \frac{p_{1,i}}{p}\right)^{-b_i} \tag{A.1}$$

$$\frac{\partial T}{\partial t}(p,r,\mu) = \left(\frac{r_0}{r}\right)^2 \times \sum\nolimits_i^N \frac{\partial T_i}{\partial t}(p,\mu) \tag{A.2}$$

We consider several orbital assumptions for Venus: no obliquity, no eccentricity and so a circular planetary orbit where r_0 is the mean Sun-Venus distance (~0.723333 AU). The cosine of the solar zenith angle $\mu = cos\ (\chi)$ is corrected for atmospheric refraction using the following function $\widetilde{\mu} = \left(\frac{1224\,\mu^2+1}{1225}\right)^{\frac{1}{2}}$. For each band i, we have: $\frac{\partial T}{\partial t}\left(p_{0,i}, r_0, 1\right)$, the solar heating rate per Earth day; $p_{0,i}$, the top pressure level, a_i, the exponent for $p_{0,i}$; m_i the exponent for the corrected solar zenith angle; $p_{1,i}$, the pressure below which non-LTE are significant; and b_i, the exponent for $p_{1,i}$. As in Gilli et al. (2021), the central pressure for transition from LTE to non-LTE radiation tendencies (ptrans) is 0.2 Pa.

First, we obtained the heating rate of each band in the Fig. 12 of Roldán et al. (2000) and the total heating rate for each solar zenith angle in the Fig. 20 of Roldán et al. (2000). From the Fig. 12 data, we used Eq. (A.1) to fit each heating rate band. Once we had a good fit for SZA = 60°, we checked if the fit is consistent with all SZA. If this was not the case, we reverted to the multiband parameterization and start again until we got a consistent fit with the SZA. Finally, the amplitude of the heating rates of each band (except 43b) was halved because the temperature became too large. This choice is justified by the fact that Roldan et al. (2000) uses the oxygen composition of VTS3 that are a factor 2 lower than (indirect) measurements of O by SPICAV above ~90 km (Soret et al., 2012). Even if there are no measurements during daytime, it is possible to assume that this "deficit" in O abundance in VTS3 produces larger heating in the Roldan et al. (2000) computations by approximately a factor two. Furthermore, the oxygen sensitivity of band 2.7 is higher than that of band 4.3 at low altitude, justifying its exclusion. The final values are presented in Table A.1. The differences between the different non-LTE CO_2 near infrared parameterizations of Gilli et al. (2017), Gilli et al. (2021) and the current study are presented in Fig. A.1.

Table A.1
Non-LTE parameterization used for each IR band (FB: Fundamental Band. FH: First hot band. ISO: Isotopic fundamental band. 43: 4.3 μm band. 43b: 4.3 μm band at lower altitude. NIR: Near InfraRed Band in the wavelength range from 1 to 2 μ).

Parameter description	FB	ISO	FH	43	43b	NIR
Solar Heating per Earth day [K/Eday]	59.5	132.5	1.25	27.5	100.	3.25
Top pressure level [Pa]	0.185	0.313	3.98	0.625	5.5	35.65
Pressure below which non-LTE are significant [Pa]	$2.9{\cdot}10^{-4}$	0.076	0.17	0.043	1.	0.046

(*continued on next page*)

Table A.1 (*continued*)

Parameter description	FB	ISO	FH	43	43b	NIR
b_i exponent	3.7	1.65	2.90	2.60	2.3	2.1
m_i exponent	0.82	0.55	0.55	0.55	0.55	0.55
a_i exponent	0.76	0.99	2.16	1.654	0.4	0.9

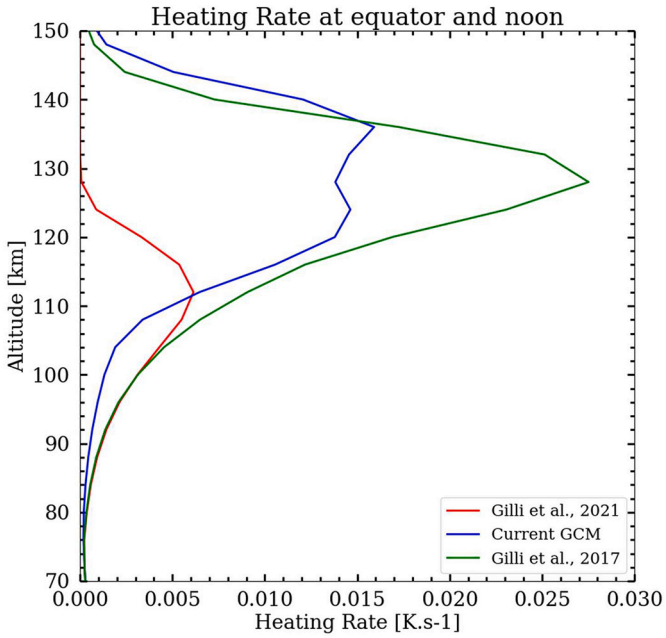

Fig. A.1. Vertical profiles of the non-LTE CO_2 near infrared heating rate at equator and noon for current (solid blue line) and previous versions (green: Gilli et al., 2017; red: Gilli et al., 2021) of the IPSL VGCM. (For interpretation of the references to colour in this figure legend, the reader is referred to the web version of this article.)

References

Bougher, S.W., Dickinson, R.E., Ridley, E.C., Roble, R.G., 1988. Venus mesosphere and thermosphere III. Three-dimensional general circulation with coupled dynamics and composition. Icarus 73, 545–573. https://doi.org/10.1016/0019-1035(88)90064-4.

Bougher, S.W., Engel, S., Roble, R.G., Foster, B., 1999. Comparative terrestrial planet thermospheres 2. In: Solar Cycle Variation of Global Structure and Winds at Equinox, vol. 104, pp. 16591–16611. https://doi.org/10.1029/1998JE001019.

Brecht, A.S., Bougher, S.W., Gérard, J.-C., Parkinson, C.D., Rafkin, S., Foster, B., 2011. Understanding the variability of nightside temperatures, NO UV and O_2 IR nightglow emissions in the Venus upper atmosphere. J. Geophys. Res. 116, E08004. https://doi.org/10.1029/2010JE003770.

Chaufray, J.-Y., Gonzalez-Galindo, F., Forget, F., Lopez-Valverde, M.A., Leblanc, F., Modolo, R., Hess, S., 2015. Variability of the hydrogen in the martian upper atmosphere as simulated by a 3d atmosphere-exosphere coupling. Icarus 245, 282–294. https://doi.org/10.1016/j.icarus.2014.08.038.

Fang, X., et al., 2018. Global simulation of Mars upper atmospheric effects of the 10 September 2017 solar flare. In: GRL Special Issue, Impact of the Sept. 10, 2017, Solar Event on Mars, 2018GL077829.

Forget, F., Hourdin, F., Fournier, R., Hourdin, C., Talagrand, O., Collins, M., Lewis, S.R., Read, P.L., Huot, J.-P., 1999. Improved general circulation models of the Martian atmosphere from the surface to above 80 km. J. Geophys. Res. 104 (E10), 24155–24175. https://doi.org/10.1029/1999JE001025.

Fox, J.L., 1988. Heating efficiencies in the thermosphere of Venus reconsidered. Planet. Space Sci. 36, 37–46. https://doi.org/10.1016/0032-0633(88)90144-4.

Fox, J.L., 2007. Near-terminator Venus ionosphere: how chapman-esque? J. Geophys. Res. 112, E04S02. https://doi.org/10.1029/2006JE002736.

Fox, J.L., Sung, K.Y., 2001. Solar activity variations of the Venus thermosphere/ionosphere. J. Geophys. Res. 106 (A10), 21305–21335. https://doi.org/10.1029/2001ja000069.

Garate-Lopez, I., Lebonnois, S., 2018. Latitudinal variation of clouds' structure responsible for Venus' cold collar. Icarus 314, 1–11. https://doi.org/10.1016/j.icarus.2018.05.011.

Garcia, R.F., Drossart, P., Piccioni, G., Lopez-Valverde, M., Occhipinti, G., 2009. Gravity waves in the upper atmosphere of Venus revealed by CO_2 nonlocal thermodynamic equilibrium emissions. J. Geophys. Res. 114, E00B32. https://doi.org/10.1029/2008JE003073.

Gilli, G., López-Valverde, M.A., Peralta, J., Bougher, S., Brecht, A., Drossart, P., Piccioni, G., 2015. Carbon monoxide and temperature in the upper atmosphere of Venus from VIRTIS/Venus express non-LTE limb measurements. Icarus 248 (478–498), 0019–1035. https://doi.org/10.1016/j.icarus.2014.10.047.

Gilli, G., Lebonnois, S., González-Galindo, F., López-Valverde, M.A., Stolzenbach, A., Lefèvre, F., Chaufray, J.-Y., Lott, F., 2017. Thermal structure of the upper atmosphere of Venus simulated by a ground-to-thermosphere GCM. Icarus 281 (55–72), 0019–1035. https://doi.org/10.1016/j.icarus.2016.09.016.

Gilli, G., Navarro, T., Lebonnois, S., Quirino, D., Silva, V., Stolzenbach, A., Lefèvre, F., Schubert, G., 2021. Venus upper atmosphere revealed by a GCM: II. Model validation with temperature and density measurements. Icarus 366, 114432. ISSN 0019-1035. https://doi.org/10.1016/j.icarus.2021.114432.

Giorgini, J., et al., 1995. Magellan aerobrake navigation. J. Brit. Interplanet. Soc. 48, 111–122. https://ui.adsabs.harvard.edu/abs/1995JBIS...48..111G.

González-Galindo, F., Forget, F., López-Valverde, M.A., Angelats i Coll, M., Millour, E., 2009. A ground-to-exosphere Martian general circulation model: 1. Seasonal, diurnal, and solar cycle variation of thermospheric temperatures. J. Geophys. Res. 114, E04001. https://doi.org/10.1029/2008JE003246.

Hedin, A.E., Niemann, H.B., Kasprzak, W.T., Seiff, A., 1983. Global empirical model of the Venus thermosphere. J. Geophys. Res. 88 (A1), 73–83. https://doi.org/10.1029/JA088iA01p00073.

Hoshino, N., Fujiwara, H., Takagi, M., Kasaba, Y., 2013. Effects of gravity waves on the day-night difference of the general circulation in the Venusian lower thermosphere. J. Geophys. Res. (Planets) 118, 2004–2015. https://doi.org/10.1002/jgre.20154.

Kasprzak, W.T., Niemann, H.B., Hedin, A.E., 1993. Wave-like perturbations observed at low altitudes by the Pioneer Venus orbiter neutral mass spectrometer during orbiter entry. Geophys. Res. Lett. 20 (A23), 2755–2758. https://doi.org/10.1029/93GL02241.

Keating, G.M., Bougher, S.W., 1992. Isolation of major Venus thermospheric cooling mechanism and implications for earth and Mars. J. Geophys. Res. 97 (A4), 4189–4197. https://doi.org/10.1029/91JA02444.

Keating, G.M., Hsu, N.C., 1993. The Venus atmospheric response to solar cycle variations. Geophys. Res. Lett. 20, 2751. https://doi.org/10.1029/93GL03010.

Keating, G.M., Nicholson, J.Y., Lake, L.R., 1980. Venus upper atmosphere structure. J. Geophys. Res. 85 (A13), 7941–7956. https://doi.org/10.1029/JA085iA13p07941.

Keating, G.M., Bertaux, J.L., Bougher, S.W., Dickinson, R.E., Cravens, T.E., Hedin, A.E., 1985. Models of Venus neutral upper atmosphere - structure and composition. Adv. Space Res. 5, 117–171. https://doi.org/10.1016/0273-1177(85)90200-5.

Kniffin, D.A., 1993. Pioneer Venus orbiter at Venus: PVO-V-POS-5–VSOCOORDS-12SEC-V1.0. In: NASA Planetary Data System, PVO-V-POS-5–VSOCOORDS-12SEC-V1.0. https://doi.org/10.17189/1519830.

Kouyama, T., Imamura, T., Taguchi, M., Fukuhara, T., Sato, T.M., Yamazaki, A., Futaguchi, M., Murakami, S., Hashimoto, G.L., Ueno, M., Iwagami, N., Takagi, S., Takagi, M., Ogohara, K., Kashimura, H., Horinouchi, T., Sato, N., Yamada, M., Yamamoto, Y., Ohtsuki, S., Sugiyama, K., Ando, H., Takamura, M., Yamada, T., Satoh, T., Nakamura, M., 2017. Topographical and local time dependence of large stationary gravity waves observed at the cloud top of Venus. Geophys. Res. Lett. 44, 12,098–12,105. https://doi.org/10.1002/2017GL075792.

Lebonnois, S., Hourdin, F., Eymet, V., Crespin, A., Fournier, R., Forget, F., 2010. Superrotation of Venus' atmosphere analyzed with a full general circulation model. J. Geophys. Res. (Planets) 115, 6006. https://doi.org/10.1029/2009JE003458.

Lebonnois, S., Sugimoto, N., Gilli, G., 2016. Wave analysis in the atmosphere of Venus below 100-km altitude, simulated by the LMD Venus GCM. Icarus 278, 38–51. https://doi.org/10.1016/j.icarus.2016.06.004.

Limaye, S.S., Lebonnois, S., Mahieux, A., Pätzold, M., Bougher, S., Bruinsma, S., Chamberlain, S., Clancy, R.T., Gérard, J.C., Gilli, G., Grassi, D., Haus, R., Herrmann, M., Imamura, T., Kohler, E., Krause, P., Migliorini, A., Montmessin, F., Pere, C., Persson, M., Piccialli, A., Rengel, M., Rodin, A., Sandor, B., Sornig, M., Svedhem, H., Tellmann, S., Tanga, P., Vandaele, A.C., Widemann, T., Wilson, C.F., Müller-Wodarg, I., Zasova, L., 2017. The thermal structure of the Venus atmosphere: intercomparison of Venus express and ground based observations of vertical temperature and density profiles. Icarus 294, 124–155. https://doi.org/10.1016/j.icarus.2017.04.020.

Lott, F., Guez, L., 2013. A stochastic parameterization of the gravity waves due to convection and its impact on the equatorial stratosphere. J. Geophys. Res. Atmos. 118, 8897–8909. https://doi.org/10.1002/jgrd.50705.

Lott, F., Guez, L., Maury, P., 2012. A stochastic parameterization of non-orographic gravity waves: formalism and impact on the equatorial stratosphere. Geophys. Res. Lett. 39, L06807. https://doi.org/10.1029/2012GL051001.

Mahajan, K.K., Kasprzak, W.T., Brace, L.H., Niemann, H.B., Hoegy, W.R., 1990. Response of Venus exospheric temperature measured by neutral mass spectrometer to solar EUV flux measured by Langmuir probe on the Pioneer Venus orbiter. J. Geophys. Res. 95 (A2), 1091–1095. https://doi.org/10.1029/JA095iA02p01091.

Mendonça, J.M., Read, P.L., 2016. Exploring the Venus global super-rotation using a comprehensive general circulation model. Planet. Space Sci. 134, 1–18. https://doi.org/10.1016/j.pss.2016.09.001.arXiv:1609.06549.

Müller-Wodarg, I.C.F., Forbes, J.M., Keating, G.M., 2006. The thermosphere of Venus and its exploration by a Venus express accelerometer experiment. Planet. Space Sci. 54, 1415–1424. https://doi.org/10.1016/j.pss.2006.04.029.

Müller-Wodarg, I., Bruinsma, S., Marty, J.C., et al., 2016. In situ observations of waves in Venus's polar lower thermosphere with Venus express aerobraking. Nat. Phys. 12, 767–771. https://doi.org/10.1038/nphys3733.

Navarro, T., Schubert, G., Lebonnois, S., 2018. Author correction: atmospheric mountain wave generation on Venus and its influence on the solid planet's rotation rate. Nat. Geosci. 11, 487–491. https://doi.org/10.1038/s41561-018-0257-7.

Navarro, T., Gilli, G., Schubert, G., Lebonnois, S., Lefevre, F., Quirino, D., 2021. Venus' upper atmosphere revealed by a gcm: I. structure and variability of the circulation. Icarus, 114400. https://doi.org/10.1016/j.icarus.2021.114400.

Niemann, H.B., et al., 1980. Pioneer Venus orbiter neutral gas mass spectrometer experiment. IEEE Trans. Geosci. Remote Sens. 1, 60–65. https://doi.org/10.1109/TGRS.1980.350282.

Persson, M., 2015. Venus Thermosphere Densities as Revealed by Venus Express Torque and Accelerometer Data. Master Thesis. Lulea Univ. of Technology.

Piccialli, A., Montmessin, F., Belyaev, D., Mahieux, A., Fedorova, A., Marcq, E., Bertaux, J.L., Tellmann, S., Vandaele, A.C., Korablev, O., 2015. Thermal Structure of Venus Nightside Upper Atmosphere Measured by Stellar Occultations with SPICAV/Venus Express, vol. 113, pp. 321–335. https://doi.org/10.1016/j.pss.2014.12.009.

Roldán, C., López-Valverde, M.A., López-Puertas, M., Edwards, D.P., 2000. Non-LTE infrared emission of CO_2 in the atmosphere of Venus. Icarus 147, 11–25. https://doi.org/10.1006/icar.2000.6432.

Rosenblatt, P., Bruinsma, S.L., Müller-Wodarg, I.C.F., Häusler, B., Svedhem, H., Marty, J.C., 2012. First ever in situ observations of Venus' polar upper atmosphere density using the tracking data of the Venus express atmospheric drag experiment (VExADE). Icarus 217 (2), 831–838. https://doi.org/10.1016/j.icarus.2011.06.019.

Scarica, P., Garate-Lopez, I., Lebonnois, S., Piccioni, G., Grassi, D., Migliorini, A., Tellmann, S., 2019. Validation of the IPSL Venus GCM thermal structure with Venus express data. Atmosphere. 10 (10), 584. https://doi.org/10.3390/atmos10100584.

Seiff, A., Schofield, J.T., Kliore, A.J., Taylor, F.W., Limaye, S.S., Revercomb, H.E., Sromovsky, L.A., Kerzhanovich, V.V., Moroz, V.I., Marov, M.Ya., 1985. Models of the structure of the atmosphere of Venus from the surface to 100 kilometers altitude. Adv. Space Res. 5 (11), 3–58. https://doi.org/10.1016/0273-1177(85)90197-8.

Soret, L., Gérard, J.-C., Montmessin, F., Piccioni, G., Drossart, P., Bertaux, J.L., 2012. Atomic oxygen on the Venus nightside: global distribution deduced from airglow mapping. Icarus 217, 849–855. https://doi.org/10.1016/j.icarus.2011.03.034.

Stolzenbach, A., Lefèvre, F., Lebonnois, S., Määttänen, A., Bekki, S., 2014. Three-dimensional modelling of Venus photochemistry. In: EGU General Assembly Conference Abstracts, p. 5315.

Stolzenbach, A., Lefèvre, F., Lebonnois, S., Maattanen, A.E., Bekki, S., 2015. Three-dimensional modelling of Venus photochemistry. In: AGU Fall Meeting Abs.

Sugimoto, N., Takagi, M., Matsuda, Y., 2014. Waves in a Venus general circulation model. Geophys. Res. Lett. 41, 7461–7467. https://doi.org/10.1002/2014GL061807.

Thuillier, G., Floyd, L., Woods, T.N., Cebula, R., Hilsenrath, E., Hersé, M., Labs, D., 2004. Solar irradiance reference spectra for two solar active levels. Adv. Space Res. 34, 256–261. https://doi.org/10.1016/j.asr.2002.12.004.

Tobiska, K.W., 2003. Forecast E10.7 for improved low-earth-orbit satellite operations. J. Spacecr. Rocket. 40 (3), 405–410. https://doi.org/10.2514/6.2002-1143.

Tobiska, W.K., et al., 2000. The SOLAR2000 empirical solar irradiance model and forecast tool. J. Atmos. Solar-Terres. Phys. 62 (14), 1233–1250. https://doi.org/10.1016/S1364-6826(00)00070-5.

Tolson, R.H., Prince, J., Konopliv, A., 2013. An atmospheric variability model for Venus aerobraking missions. AAIA. https://doi.org/10.2514/6.2013-4830.

Yamamoto, M., 2019. Equatorial kelvin-like waves on slowly rotating and/or small-sized spheres: application to Venus and titan. Icarus 322, 103–113. https://doi.org/10.1016/j.icarus.2019.01.008.

Zalucha, A.M., Brecht, A.S., Rafkin, S., Bougher, S.W., Alexander, M.J., 2013. Incorporation of a gravity wave momentum deposition parameterization into the Venus thermosphere general circulation model (VTGCM). J. Geophys. Res. (Planets) 118, 147–160. https://doi.org/10.1029/2012JE004168.